https://doi.org/10.5194/gmd-2022-92
Preprint. Discussion started: 24 May 2022

Geoscientific Model Development Discussions

An Improved Algorithm for Simulating Surface Flow Dynamics based on the Flow-Path Network Model

Qianjiao Wu[1,3], Yumin Chen[2], Huaming Xie[1,3], Tong Xu[4], Jiayong Yu[5], Ting Zhang[1,3]

[1] School of Environment and Energy Engineering, Anhui Jianzhu University, Hefei, 230601, China
[2] School of Resource and Environment Science, Wuhan University, Wuhan, 430079, China
[3] Institute of Remote Sensing and Geographic Information Systems, Anhui Jianzhu University, Hefei, 230601, China
[4] School of Architecture and Urban Planning, Anhui Jianzhu University, Hefei, 230601, China
[5] School of Civil Engineering, Anhui Jianzhu University, Hefei, 230601, China;

Correspondence to: Qianjiao Wu (qianjiaowu@ahjzu.edu.cn)

Abstract. This paper proposes an improved algorithm for simulating the surface flow dynamics based on the flow-path network model. This algorithm utilizes the parallel-multi-point method to extract the critical points and the D8 algorithm to retrieve the drainage networks from the regular-grid digital elevation model (DEM) for constructing a drainage-constrained triangulated irregular network (TIN). Then, it combines the flow directions of triangular facets over TIN with resampled flow source points to track flow lines to generate the flow path network (FPN) based on the flow-path network model. On this basis, the proposed algorithm employs three terrain parameters (slope length factor, topographic wetness index and flow path curvature) to improve the classical Manning equation based on the analytic hierarchy process (AHP) to enhance the accuracy of the flow velocity calculation. The topographic wetness index and flow path curvature are derived by the flow-path-network-triangular-facet-network (FPN_TFN) algorithm, a new flow-path-network-topographic-wetness-index (FPN_TWI) algorithm and the flow-path-network-flow-path-curvature (FPN_C) algorithm, respectively. Finally, the velocity estimation function and surface flow discharge simulation function are parallelized by the Compute Unified Device Architecture (CUDA) to enhance its computational efficiency. The outcomes are compared with the algorithm before improvement (TIN_based algorithm) and the SWAT model. The results demonstrate that the speedup ratio reaches 15.7 compared to the TIN_based algorithm. The Nash coefficient increases by 6.49%, the correlation coefficient decreases slightly, and the balance coefficient increases by 19.08%. Compared with the SWAT model, the Nash coefficient and correlation coefficient increase by 97.56% and 4.60%, respectively. The balance coefficient is close to 1 and outperforms the compared algorithms.

https://doi.org/10.5194/gmd-2022-92
Preprint. Discussion started: 24 May 2022


Geoscientific Model Development Discussions

1 Introduction

Due to the evolution of the natural environment, the change in climate and human activities and the decrease in vegetation coverage, the rapid surface flow in the event of continuous heavy rainfall or storms is very likely to cause flood disasters, which will cause direct or potentially significant harm to people's lives, social production and the natural environment (Easterling et al., 2000). Therefore, accurately and immediately simulating the surface flow dynamics is an urgent task to be solved in disaster prevention and mitigation. It has an important value in the applications of national construction and lays a foundation for scientific land planning, environmental protection, water resource management and natural disaster response.

The keys to simulating the surface flow dynamics are effectively modelling the terrain surface, accurately calculating the flow velocity and quickly simulating the dynamic process. In terms of terrain surface modelling, the regular-grid digital elevation model (DEM) is widely utilized to describe terrain surfaces during the simulation of surface flow dynamics (Chen et al., 2014; Maneta and Wallender, 2013; Zhang et al., 2018; Zhou and Liu, 2006), such as the classical TOPMODEL (Beven and Kirkby, 1979) and Soil and Water Assessment Tool (SWAT) models (Arnold et al., 1998; Hellmers and Frohle, 2022). Although regular-grid DEMs can better describe continuous terrain surfaces, regular-grid DEMs have the same grid size, so it is difficult to fully and accurately express complex and changeable terrain surfaces, leading to the uncertainty of retrieving the critical points, lines and terrain parameters from regular-grid DEMs (David and Frank, 2013; Glenn and Ashton, 2012; Zhou and Liu, 2004). In the simulation of surface flow dynamics, it is still difficult to select the appropriate grid resolution of regular-grid DEMs (Thavhana et al., 2018). The coarser resolution easily leads to misjudgment of important critical points and lines and makes it difficult to obtain real terrain parameters, which has an important effect on the flow velocity. The finer resolution can easily lead to a large amount of computation, which is difficult to apply in large watersheds.

The triangulated irregular network (TIN) can avoid the above-mentioned drawbacks of the regular-grid DEM and replace it for simulating the surface flow dynamics, using models such as the Geomorphic Information System (BGIS) model (Tachikawa et al., 1994), Channel-hillslope Integrated Landscape Development (CHILD) model (Tucker et al., 2001), and high-performance TIN-based model (Zhang et al., 2016) and so on. When TIN is used to describe the terrain surface, the method of simulating the surface flow dynamic has certain advantages, such as adaptive resampling of terrain surface, better expression of complex and changeable surface, determination of flow direction not restricted by grid data structure and so on. However, the simulation process is complex and greatly limited in large watershed applications (Chen et al., 2014; Ivanov et al., 2004; Staškovanová and Minár, 2016; Swarnkar et al., 2018; Tachikawa and Takasao, 1996). Therefore, the contradiction between the existing terrain surface representation model and the requirement of simulating the surface flow dynamics is quite prominent.

Both regular-grid DEM and TIN only describe the terrain surface but cannot reflect the surface flow dynamics. In the early stage, simplified empirical formulas were utilized to simulate the dynamic process (Jia et al., 2005). With the development of digital terrain modelling and numerical analysis, it is possible to predict surface flow dynamics based on

https://doi.org/10.5194/gmd-2022-92
Preprint. Discussion started: 24 May 2022

physical models under certain environmental conditions (Bourdin et al., 2012; Wilson and Gallant, 2000; Zhang et al., 2018). Critical to the simulation of surface flow dynamics is accurately calculating the velocity of surface flow (Djokic and Maidment, 1993).

Beven et al. (1980) used the finite element method to simulate the movement of surface and ground flow. Tachikawa et al. (1994) utilized the cubic spline function to draw the slope of a three-dimensional model for simulating the one-dimensional surface flow dynamics. Shen et al. (1995) explored the water balance equation and Muskingum method to simulate runoff and surface flow discharge at any position and time. Arnold et al. (1998) used the SCS curve method to simulate the runoff discharge within each HRU and accumulated the separate discharge to obtain the total runoff of the basin. Then, the variable storage coefficient method was applied to carry out surface flow discharge. Olivera and Maidment (2000) adopted the parameters of drainage networks and hydrological systems to simulate runoff and surface flow dynamics. Qu and Duffy (2007) applied the semidiscrete finite volume method (FVM) to couple hydrological processes, generated the optimal Delaunay triangulation network according to the given constraints and simulated the surface flow dynamics based on the approximate equation of a two-dimensional diffusion wave. López-Vicente et al. (2013) utilized eight different cumulative flow calculation methods to simulate the surface flow dynamics of different spatial modes. These methods can only simulate the surface flow dynamics of a limited number of points, such as the outlet of a basin or several points within a subbasin, based on empirical formulas or traditional hydrological analysis methods, so it is difficult to simulate the real-time changes in surface flow discharge at any location, and the accuracy still needs to be improved.

Compared with the abovementioned methods, Chen et al. (2014) utilized a flow-path network model to simulate the surface flow dynamics based on the drainage-constrained TIN (referred to as the TIN_based algorithm) and verified its accuracy and feasibility. This method identified the flow direction of each triangular facet over the TIN based on its fixed slope and aspect. Then, it combined the flow direction with the resampled flow source points to track the flow path along the TIN surface and employed the Manning formula to ascertain the flow velocity for simulating the surface flow discharge at any location. However, the method only considers the impact of slope on the flow velocity and does not consider the influence of other terrain parameters (such as slope length factor, topographic wetness index, flow path curvature, upslope slope and upslope area) on the flow velocity. The existing methods of deriving these terrain parameters usually utilize an analysis window or local interpolation on a regular grid DEM, whose accuracy depends on the DEM resolution, analysis window and interpolation method. They may lead to the deviation of terrain parameter derivation, and the analysis window or local interpolation method may affect the accuracy of surface flow dynamics simulation.

In addition, parallel computing has been employed to describe the terrain surface based on regular-grid DEM/TIN (Blaszczak-Bak et al., 2018; Puppo et al., 1994; Zhou et al., 2017) and simulate the surface flow dynamics (Chaney et al., 2015; Zhang et al., 2016; Kuffour et al., 2020) Compared with multicore CPU parallel computing, GPU parallel computing can perform the parallel computing of extremely large data and make it possible to improve the performance of high-performance processing and computing efficiency on a single computer (Wu et al., 2019). The compute unified device architecture (CUDA) performs on the GPU in a generic fashion and can efficiently solve more computations (NVIDIA

https://doi.org/10.5194/gmd-2022-92
Preprint. Discussion started: 24 May 2022

Corporation, 2015).

Therefore, this paper aims to propose an improved algorithm for simulating the surface flow dynamics based on a flow-path network model with a high accuracy and real-time response efficiency. This algorithm can quickly construct the drainage-constrained TIN by inserting the drainage into the critical points extracted from the regular-grid DEM, determine the sole flow direction of each triangular facet over the TIN and track the flow lines from the randomly sampled flow source points to the drainage outlet to simplify the three-dimensional surface into a one-dimensional flow path network (FPN). On this basis, more accurate terrain parameters (slope length factor, topographic wetness index and flow path curvature) are derived from the FPN by different methods, and the classical Manning formula is improved by using terrain parameters to estimate the velocity of each flow line. Combining flow velocity with the preset travel time can simulate the surface flow discharge at any location. Finally, CUDA is used to parallelize the velocity estimation function and the surface flow discharge simulation function to quickly realize the simulation of surface flow dynamics. It can provide decision support and a scientific theoretical basis for regional land planning, environmental protection, water resource management and natural disaster response countermeasures.

2 Methodology

The methodology has four major parts: (1) generating a flow path network (FPN); (2) improving Manning's equation by combining the FPN and three terrain parameters (slope length factor, topographic wetness index and flow path curvature); (3) simulating the spatial–temporal dynamics of surface flow based on the improved Manning's equation; and (4) evaluating the accuracy and computational efficiency of the improved algorithm. The detailed procedures of the improved algorithm are shown in Fig. 1.

https://doi.org/10.5194/gmd-2022-92
Preprint. Discussion started: 24 May 2022

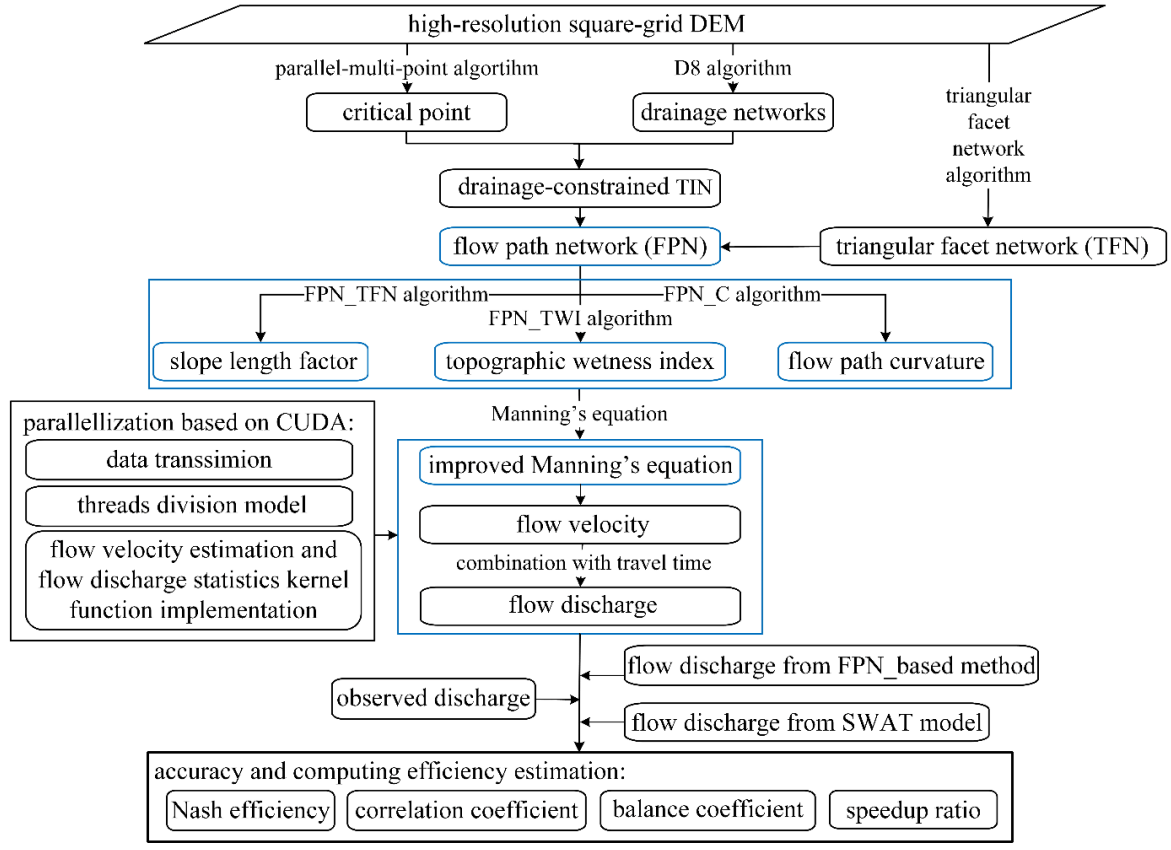

Figure 1: Detailed procedures of the improved algorithm for simulating the surface flow dynamics based on the flow-path network model.

2.1 Generating a flow path network (FPN)

The flow-path network model (Chen et al., 2014) is employed to generate a flow path network (FPN). The model consists of four steps, as illustrated in Fig. 1.

First, The high accuracy and computational efficiency of the parallel-multi-point algorithm (Wu et al., 2019), is utilized to extract the critical points from a no-depression DEM during the generation of the FPN. Zhou and Chen (2011) and Wu et al. (2021) had already proven that the drainage networks extracted by the D8 method (O'Callaghan and Mark, 1984) are inserted as the constrained edges into the critical points to build a high-accuracy TIN. Therefore, the D8 method is used to obtain the drainage networks in the improved method.

Second, the compound method (Zhou and Chen, 2011) is used to generate the drainage-constrained TIN by combining the retrieved critical points and drainage networks. In addition, to avoid narrow triangular facets over the TIN, the distances between the critical points and between the critical points and drainage networks are expected to be greater than the DEM resolution (Wu et al., 2020, 2021) because the long-narrow triangular facet is averse to determine the flow direction depending on the aspect and slope and still increases the volume calculation during the generation of the FPN.

https://doi.org/10.5194/gmd-2022-92
Preprint. Discussion started: 24 May 2022


Geoscientific Model Development Discussions

Third, the resampling method was used to obtain the flow source points from the no-depression DEM. A random point in each regular grid over the DEM is regarded as a flow source point, and each flow source point describes the start point of flow lines over the FPN. Then, the aspect and slope of each triangular facet are calculated by the coordinates of the three corners of the facet, and the flow direction of each triangular facet can be determined by its aspect and slope (Chen et al., 2014). Finally, a flow line starting from a flow source point can be tracked by combining the flow source point and the flow directions of all the triangular facets over the TIN. The tracking algorithm is described in detail by Chen et al. (2014). We construct the topological relationship between the flow lines to generate a flow path network (FPN).

2.2 Improving Manning's equation by combining the FPN and three terrain parameters (slope length factor, topographic wetness index and flow path curvature)

Considering the influence of the terrain parameters on the velocity of the surface flow, we use three parameters (slope length factor, topographic wetness index and flow path curvature) to improve Manning's equation to enhance the velocity accuracy of the surface flow.

2.2.1 Obtaining the terrain parameters (slope length factor, topographic wetness index and flow path curvature) from the FPN

The Manning's equation had been proposed by Manning (1891) to estimate flow velocity of an open channel based on the empirical research. The empirical equation is a widely used formula and it can be expressed as follows:

$$v = \frac{R^{2/3} * S^{1/2}}{n}, \quad (1)$$

During the simulation of the surface flow dynamics, Manning's roughness coefficient changes with the vegetation cover type, and the hydraulic radius can approach the runoff depth (Chen et al., 2014). The runoff depth can be estimated by the cumulative discharge, flow velocity and DEM resolution and can be expressed as Eq. (2). Eq. (1) and Eq. (2) are carried out iteratively to simulate the flow velocity and surface flow discharge until the end of simulation.

$$h = \frac{Q}{v * g}, \quad (2)$$

where h denotes the runoff depth (m3/s), Q denotes the flow velocity (m/s), g denotes the grid cell (m).

Manning's equation only considers the influence of slope on flow velocity and does not consider the influence of other topographic parameters on flow velocity. For example, the slope length factor can quantify the degree of soil erosion caused by topography to accelerate the surface flow; the topographic wetness index can quantify the cumulative discharge trend and local slope to accelerate the surface flow; and the flow path curvature can quantify the degree of swing of the flow lines to hinder the surface flow. Therefore, we hope to take into account the influence of the slope length factor, topographic wetness index (TWI) and flow path curvature on flow velocity to improve the accuracy of surface flow dynamic simulation anywhere

https://doi.org/10.5194/gmd-2022-92
Preprint. Discussion started: 24 May 2022


Geoscientific Model Development Discussions

160 on the terrain surface. Meanwhile, three parameters are used to improve Manning's equation

The high accuracy and beneficial spatial distribution of the flow-path-network-triangular-facet-network (FPN_TFN) algorithm presented by Wu et al. (2021), is employed to obtain the slope length factor from a no-depression DEM. The high accuracy of the flow-path-network-flow-path-curvature (FPN_C) algorithm proposed by (Wu et al., 2020), is utilized to obtain the flow path curvature from a no-depression DEM.

165 In this study, a flow-path-network-topographic-wetness-index (FPN_TWI) algorithm is proposed to calculate the TWI from the no-depression DEM. The TWI calculation consists of slope computation, SCA estimation and TWI calculation.

(1) Slope computation

In this paper, the TFN_slope algorithm is utilized to compute the slope from a triangular facet network (TFN). The algorithm considered the constant slopes of the triangular facets over the TFN constructed from the no-depression DEM by 170 the TFN algorithm (Zhou et al., 2011). The TFN_slope method is advanced to calculate the cell's slope by averaging the slopes of all the triangular facets, which treats the grid cell as the vertex.

(2) SCA estimation

The SCA is obtained by combining the flow accumulation estimated from the TFN with the aspect evaluated by a new algorithm. The TFN is designed to simulate the flow accumulation at each cell. This estimation consists of three processes: a) 175 calculating the aspect and slope of the triangular facets over the TFN to obtain flow directions; b) tracking the flow lines by combining the flow source points that are the centres of gravity for the triangle facets with flow directions; and c) counting the number of flow lines through the grid cell to acquire the flow accumulation. These steps have been described in detail by Zhou et al. (2011).

To compute the aspect, a new algorithm is proposed, the principle of which is similar to that of the TFN_slope 180 algorithm. Considering the constant aspect of the triangular facets over the TFN, the aspect of a grid cell is the average of the aspects of all the triangular facets that treats the cell as a vertex (as shown in Eq. (3)).

$$A = \frac{A_1+A_2+\cdots+A_n}{n}, 1 \le n \le 8, \quad (3)$$

where A denotes the aspect of the grid cell, A_n denotes the aspect of the triangular facet and n denotes the nth triangular facet.

Using the flow accumulation and aspect determined above, the SCA is calculated by Eq. (4) as reported by Costa- 185 Cabral and Burges (1994).

$$SCA = \frac{S\times A}{\Delta x|sin\alpha|+\Delta y|cos\alpha|} = \frac{S\times A}{d(|sin\alpha|+|cos\alpha|)} = \frac{d\times A}{2(|sin\alpha|+|cos\alpha|)}, \quad (4)$$

where SCA denotes the specific catchment area at a grid cell; S denotes the area of the triangular facet; A denotes the flow accumulation; Δx and Δy denote the size of the grid cell in the x and y directions, respectively; d denotes the size of the grid cell; α denotes the aspect of the grid cell. In this paper, Δx and Δy are equal to d, and S is equal to $\frac{d^2}{2}$.

190 **(3) TWI calculation**

https://doi.org/10.5194/gmd-2022-92
Preprint. Discussion started: 24 May 2022


Geoscientific Model Development Discussions

Using the slope and SCA determined above, the TWI is estimated by the definition reported by Beven and Kirkby (1979) as Eq. (5).

$$TWI = ln\frac{SCA}{\tan\beta}, \quad (5)$$

where TWI denotes the topographic wetness index, SCA denotes the specific catchment area (m^2) and β denotes the slope (m/m).

2.2.2 Improving Manning's equation based on the analytic hierarchy process (AHP)

In the improved method, the slope length factor, topographic wetness index and flow path curvature are used to improve the Manning formula. The improved Manning formula is as follows:

$$v = \frac{R^{2/3}*(w_1*T+w_2*L-w_3*|C|+w_4*S)^{1/2}}{n}, \quad (6)$$

where v denotes the flow velocity (m/s), R denotes the hydraulic radius (m), T denotes the topographic wetness index (dimensionless), L denotes the slope length factor (dimensionless), C denotes the flow path curvature (m^{-1}), S denotes the slope (m/m), w_1, w_2, w_3, w_4 are the weight coefficients of the slope length factor, topographic wetness index, flow path curvature, respectively and slope and n denotes the Manning's roughness coefficient (dimensionless). The slope length factor, topographic wetness index and flow path curvature are normalized to avoid large fluctuation of flow velocity before simulating the surface flow dynamics.

In this paper, the slope length factor, topographic wetness index, flow path curvature and slope are weighted by the analytic hierarchy process (AHP). The weight determination process consists of judgment matrix construction, consistency testing and weight determination.

(1) Judgment matrix construction

The judgment matrix is constructed according to the proportional scale (Table 1) and the priority importance of the slope length factor, topographic wetness index, flow path curvature and slope to flow velocity, as shown in Matrix [1].

Table 1: The proportional scale between the different factors.

The importance of one factor to another factor	*Equal importance*	*Slight importance*	*Stronger importance*	*Intense importance*	*Extreme importance*	*Middle value of two adjacent judgments*
Quantized value	1	3	5	7	9	2, 4, 6, 8

$$\begin{bmatrix} Quantized\ value & T & L & C & S \\ T & 1 & 1/5 & 1/6 & 1/7 \\ L & 5 & 1 & 1/3 & 1/5 \\ C & 6 & 3 & 1 & 1/3 \\ S & 7 & 5 & 3 & 1 \end{bmatrix}, \quad [1]$$

https://doi.org/10.5194/gmd-2022-92
Preprint. Discussion started: 24 May 2022


Geoscientific Model Development Discussions

(2) Consistency test

Whether the judgment matrix can pass the consistency test is judged by the test coefficient of the matrix. If the test coefficient is less than 0.1, the matrix is deemed to pass the consistency test; otherwise, it is not satisfactorily consistent. The test coefficient of the matrix is calculated according to Eq. (7) and Eq. (8). The test coefficient of Matrix (1) is 0.0876, so the judgment matrix passes the consistency test.

$$CI = (\lambda - n)/(n - 1), \quad (7)$$

$$CR = CI/RI, \quad (8)$$

where CI denotes the coincidence indicator, λ denotes the maximum eigenroot of a matrix, n denotes the matrix order, RI denotes random consistency index and CR denotes the test coefficient. RI varies with the matrix order, as shown in Table 2.

Table 2: The standard value of the random consistency index.

Matrix order	1	2	3	4	5	6	7	8	9	10
RI	0	0	0.58	0.90	1.12	1.24	1.32	1.41	1.45	1.49

(3) Weight determination

According to the judgment matrix, we calculate the eigenvalues and eigenvectors and choose the maximum eigenvalue. The different weights of the slope length factor, topographic wetness index, flow path curvature and slope are equal to the elements of the eigenvector corresponding to the maximum eigenvalue. Therefore, w_1, w_2, w_3 and w_4 are 0.0563, 0.1310, 0.2388 and 0.5738, respectively.

2.3 Simulating the temporal–spatial dynamics of surface flow based on the improved Manning's equation

The improved method simulates the surface flow dynamics based on a one-dimensional flow path network (FPN), as shown in Fig. 2. It estimates the flow velocity along the flow line to the watershed outlet based on the improved Manning's equation. The surface flow discharge anywhere is simulated by combining the flow velocity with the travel time. Among them, the flow velocity estimation function and surface flow discharge count function on the flow lines over the FPN are time-consuming and parallel.

https://doi.org/10.5194/gmd-2022-92
Preprint. Discussion started: 24 May 2022

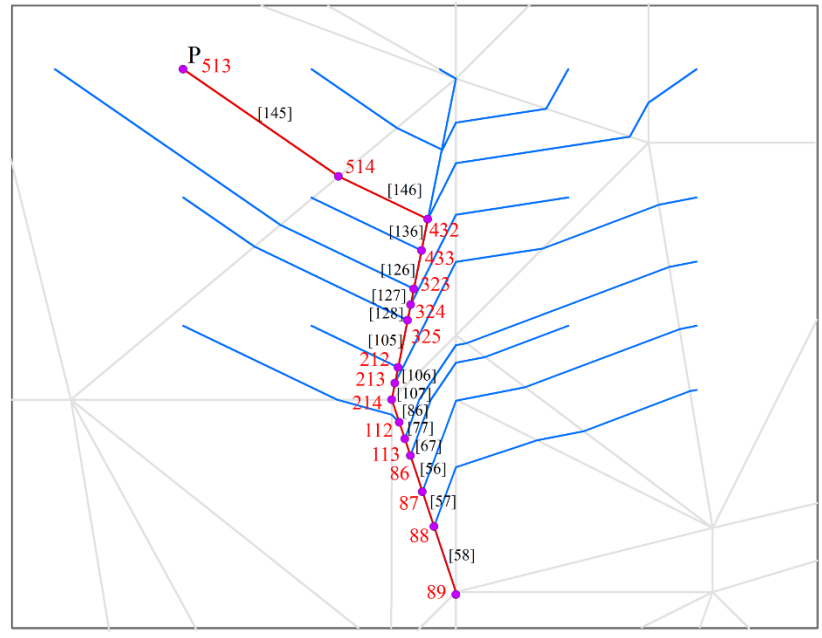

Node table

Node ID	X(m)	Y(m)	Z(m)	…
89	596079.836	5216855.423	157.44	…
88	596078.137	5216860.712	158.45	…
87	596077.233	5216863.422	159.37	…
…	…	…	…	…

Line table

Line ID	Start node	End node	s	L	T	C	Velocity(m/s)
58	88	89	32	25	14	8	v(r,s,L,T,C,n)
57	87	88	28	19	10	7	v(r,s,L,T,C,n)
56	86	87	16	7	5	3	v(r,s,L,T,C,n)
67	113	86	10	1	2	-2	v(r,s,L,T,C,n)
…	…	…	…	…	…	…	…

$v = f(r, s, L, T, C, n)$

Figure 2: Simulating the surface flow dynamics based on a one-dimensional flow path network (FPN).

Therefore, the two functions are converted into the velocity estimation kernel function and flow discharge count kernel function based on CUDA to enhance the computing efficiency. The whole parallelization process is similar to that of the parallel algorithm proposed by Wu and Chen (2020) and mainly includes data transmission, thread partition mode in CUDA and kernel function implementation. The concrete parallel processes were described in detail by Wu and Chen (2020).

2.4 Evaluating the accuracy and computational efficiency of the improved method

In this study, the Nash efficiency (N), correlation coefficient (R) and balance coefficient (B) were utilized to assess the improved algorithm's accuracy. The Nash efficiency is used to calculate the flow discharge by the impulse function instead of the net rainfall of the unit hydrograph. The correlation coefficient is a nondeterministic relationship that describes the degree of linear correlation between two variables. The balance coefficient estimates the potential deviation of the improved algorithm. For the three statistical indicators, a value close to 1 represents high accuracy. The N, R and B are expressed as follows:

$$N = 1 - \frac{\sum_{t=1}^{n}(Q_o^t - Q_m^t)^2}{\sum_{t=1}^{n}(Q_o^t - \overline{Q_o})^2}, \quad (9)$$

$$R = \frac{\sum_{t=1}^{n}(Q_m^t - \overline{Q_m}) * (Q_o^t - \overline{Q_o})}{\sqrt{\sum_{t=1}^{n}(Q_m^t - \overline{Q_m})^2 * \sum_{t=1}^{n}(Q_o^t - \overline{Q_o})^2}}, \quad (10)$$

$$B = \frac{\sum_{t=1}^{n} Q_o^t}{\sum_{t=1}^{n} Q_m^t}, \quad (11)$$

https://doi.org/10.5194/gmd-2022-92
Preprint. Discussion started: 24 May 2022

Geoscientific Model Development Discussions

where t denotes the time, Q_o^t denotes the measured flow discharge of the observation station at the time, Q_m^t denotes the simulated flow discharge at the time, $\overline{Q_o}$ denotes average value of measured flow discharge and $\overline{Q_m}$ denotes the average value of the simulated flow discharge.

In addition, the speedup ratio (r) was utilized to measure the computing efficiency of the improved method, and a larger value indicates higher computing efficiency. It can be expressed as follows:

$$r = \frac{t_c}{t_p}, \tag{12}$$

where t_c denotes the computing time of the compared algorithm, t_p denotes the computing time of the improved algorithm.

3. Experiments and Results

To assess the accuracy and computing efficiency of the improved method, the Black Brook Watershed (BBW) was selected as the experimental region. It is located in north-western New Brunswick, Canada. A 5 m DEM of the BBW region obtained through Lidar is used in this study, as shown in Fig. 3. The DEM is composed of 1,284 × 942 grid cells with elevations between 151.59 m and 240.70 m. The region is located at 47°05'N-47°09'N and 67°43'W-67°48'W, covering an area of approximately 13 km^2. The average monthly precipitation increased from 64.6 mm in February to 111.6 mm in July, with an average monthly rainfall of approximately 91 mm. The watershed is characterized by complex terrain, high-density erosion and the potential threat of heavy rainfall and snowfall to soil erosion. In the early 1990s, monitoring stations established long-term meteorological and surface flow monitoring points in the BBW, and land-use classification and management practice data of various fields in the BBW were also recorded.

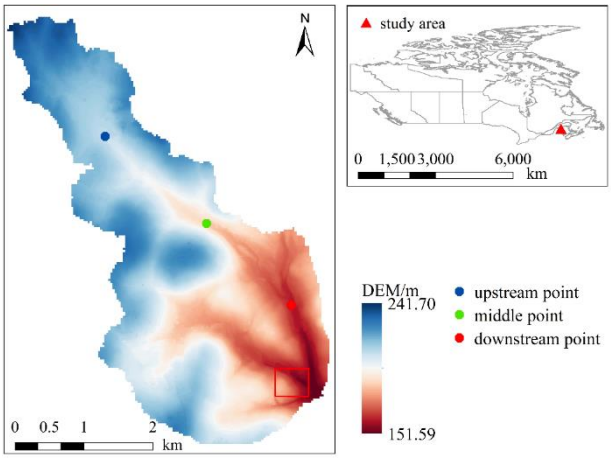

Figure 3: The test DEM of the BBW used in this study.

The experiment uses the daily runoff discharge of BBW in 2001 to simulate the daily surface flow discharge. The daily runoff discharge is simulated by the SWAT model according to the daily rainfall, and the data have a high accuracy (Chen et

https://doi.org/10.5194/gmd-2022-92
Preprint. Discussion started: 24 May 2022

Geoscientific Model Development Discussions

al., 2014). Daily rainfall data are measured data provided by the BBW Watershed Monitoring Station. Before the experiment, ArcGIS Desktop 10.2 was used to prefill the DEM image.

The different critical points were extracted from the no-depression DEM using different thresholds of 0.5, 1.0, 1.5, 2.0 and 2.5 m by the parallel-multipoint algorithm. The threshold of 2000 m^2 was used to extract the drainage networks by the D8 algorithm in this paper. The root mean square error (RMSE) of drainage-constrained TIN slightly increases when the threshold of extracting the drainage networks is greater than 2000 m^2. The threshold of 8 m was used to filter the critical point because the greater threshold value basically keeps the RMSE of drainage-constrained TIN unchanged. The drainage-constrained TINs were built by inserting the extracted drainage networks into the retrieved critical points under the different thresholds. When the threshold of 0.5 m was used to retrieve the critical points from the 5 m DEM, the number of critical points was 10,859 (Fig. 4(a)), and the number of triangular facets over the drainage-constrained TIN was 23,348 (Fig. 4(b)).

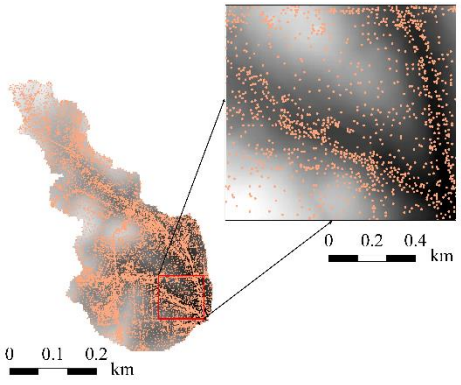

(a) critical points

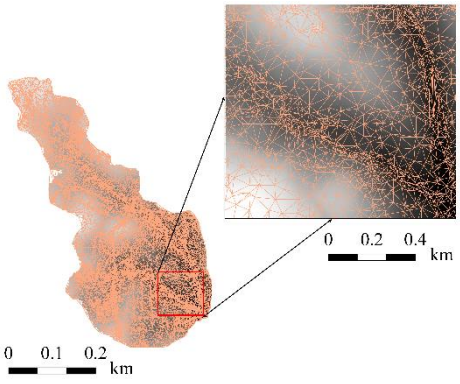

(b) drainage-constrained TIN

Figure 4: The critical points and drainage-constrained TIN from the BBW (threshold of retrieving the critical points is 0.5 m).

The 5 m DEM was resampled to DEMs of 10, 15, 20, 25 and 30 m. The random points in each regular grid over the different DEMs are regarded as the flow source points at different scales. Combining the same drainage-constrained TIN with the flow source points with different scales to generate the different FPNs (Fig. 5), the number of flow lines over the different FPNs was 134,380, 59,716, 33,634, 21,491 and 14,920.

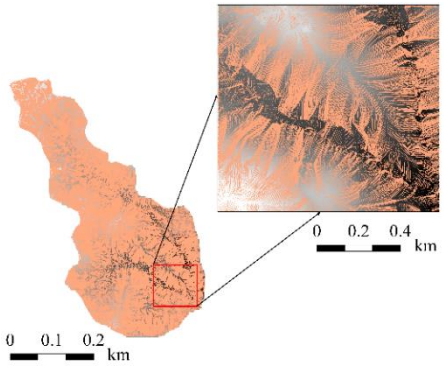

(a) the scale of flow source points = 10m

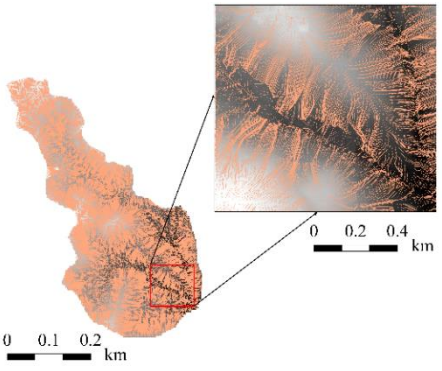

(b) the scale of flow source points = 15m

https://doi.org/10.5194/gmd-2022-92
Preprint. Discussion started: 24 May 2022

Geoscientific Model Development Discussions

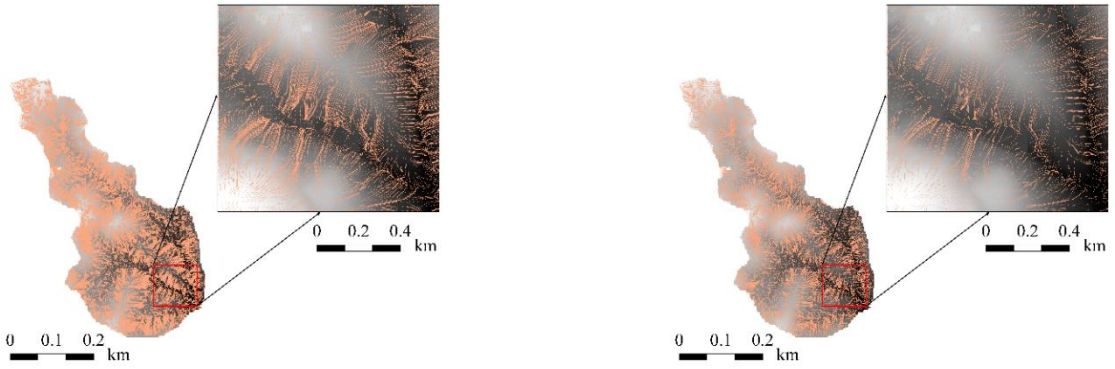

(c) the scale of flow source points = 20m (d) the scale of flow source points = 30m

Figure 5: FPNs under the flow source points with different scales (threshold of retrieving the critical points is 0.5 m).

The different slope length factor values of 10, 15, 20, 25 and 30 m were obtained from the DEMs by the FPN_TFN algorithm. The different topographic wetness index values of 10, 15, 20, 25 and 30 m were obtained from the DEMs by the FPN_TWI algorithm. The different flow path curvature values of 10, 15, 20, 25 and 30 m were obtained from the DEMs by the FPN_C algorithm, and the required threshold of cutting the flow lines was 100 m. Figure 6 illustrates the slope length factor, topographic wetness index and flow path curvature obtained from the 10 m DEM. The Manning's roughness coefficient in the improved Manning formula is determined to be 0.4 according to the land-use types of the BBW region (Chen et al., 2014), as shown in Table 3, and the values presented by Thompson (1999).

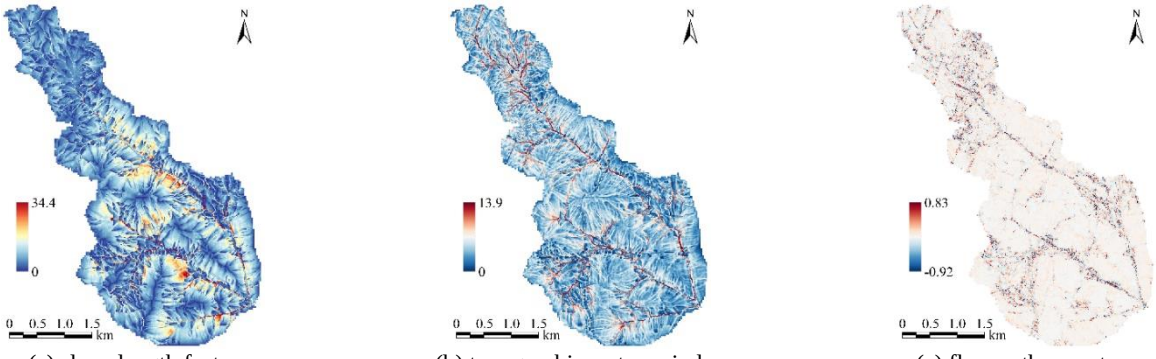

(a) slope length factor (b) topographic wetness index (c) flow path curvature

Figure 6: The slope length factor, topographic wetness index and flow path curvature obtained from the 10 m DEM.

https://doi.org/10.5194/gmd-2022-92
Preprint. Discussion started: 24 May 2022


Geoscientific Model Development Discussions

Table 3: The data for the land-use types of the BBW region.

Data	Description
Land use	Potato 32% Barley 23% Forest 22% Residents 5.3% Other's agriculture land 6.1% Others 11.6%
Climate	Wind speed Solar radiation Daily precipitation Relative humidity Maximum and minimum air temperature
Soil	AAFC detailed soil survey map

300

The improved method was utilized to simulate the surface flow dynamics at different times with a threshold of 0.5 m for retrieving the critical points and a flow source point scale of 30 m to verify its real-time dynamic simulation ability. Figure 7 shows the change in surface flow discharges from the 80th day to the 85th day in one day intervals. As shown in Fig. 7, during the observation period, the surface flow occurred in an uneven confluence to shape the outline of the stream. Later, 305 the surface flow discharge in the upstream segment starts to disappear, and the surface flow discharge in the downstream segment decreases. On the 85th day, the surface flow discharge disappeared almost completely.

https://doi.org/10.5194/gmd-2022-92
Preprint. Discussion started: 24 May 2022

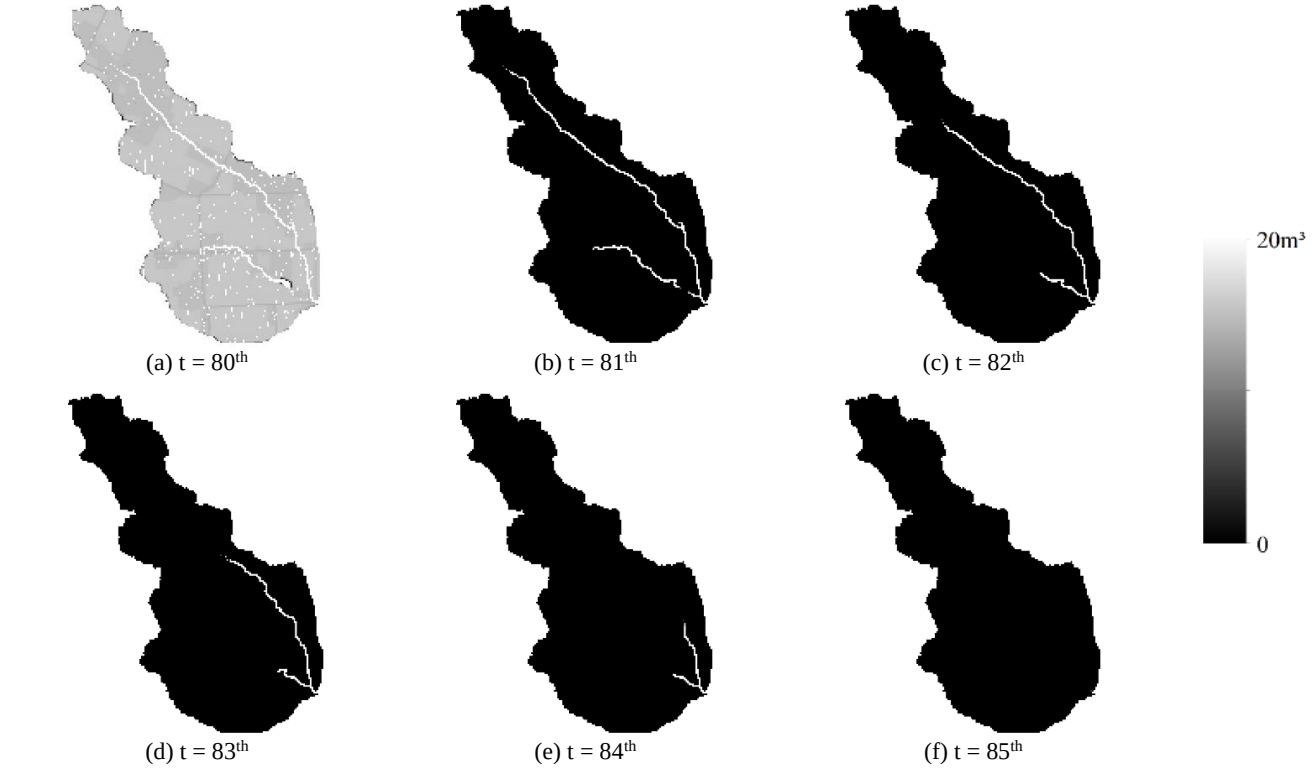

(a) t = 80th (b) t = 81th (c) t = 82th

(d) t = 83th (e) t = 84th (f) t = 85th

Figure 7: The change of surface flow discharges from 80th days to 85th days in an interval of one day (the threshold of retrieving the critical points was 0.5 m and the scale of flow source points was 30 m).

Comparing the improved algorithm with the TIN-based algorithm, the three statistical indicators were calculated by the surface flow discharge simulation under different thresholds of retrieving the critical points and scales of flow source points at the outlet of the BBW. Table 4 shows the three statistical indicators from the improved algorithm and TIN-based algorithm. To evaluate the accuracy of the improved algorithm, it was compared with the SWAT model under a flow source point scale of 30 m at the outlet of the BBW. Table 5 shows three statistical indicators from the SWAT model. Figure 8 illustrates the surface flow discharge simulated from the SWAT model and improved algorithm under the threshold of 0.5 m of retrieving the critical points and flow source points at a scale of 30 m at the outlet of the BBW.

https://doi.org/10.5194/gmd-2022-92
Preprint. Discussion started: 24 May 2022

Geoscientific Model Development Discussions

320 **Table 4: Three statistical indicators from the improved algorithm and TIN_based algorithm under different thresholds of retrieving the critical points and scales of flow source points at the outlet of the BBW.**

Threshold/m	Algorithm	Statistical indicators	Scale of the flow source points/m				
			10	15	20	25	30
0.5	TIN_based	*N*	0.77	0.77	0.77	0.77	0.77
		R	0.91	0.91	0.91	0.91	0.91
		B	1.30	1.31	1.31	1.30	1.30
	Improved algorithm	*N*	0.81	0.81	0.81	0.82	0.81
		R	0.90	0.90	0.90	0.91	0.90
		B	1.08	1.08	1.08	1.11	1.08
1.0	TIN_based	*N*	0.77	0.77	0.77	0.77	0.77
		R	0.91	0.91	0.91	0.91	0.91
		B	1.31	1.31	1.31	1.31	1.31
	Improved algorithm	*N*	0.81	0.81	0.81	0.82	0.80
		R	0.90	0.90	0.90	0.90	0.90
		B	1.08	1.10	1.10	1.11	1.07
1.5	TIN_based	*N*	0.77	0.77	0.77	0.77	0.77
		R	0.91	0.91	0.91	0.91	0.91
		B	1.31	1.31	1.32	1.32	1.31
	Improved algorithm	*N*	0.81	0.81	0.81	0.81	0.81
		R	0.90	0.90	0.90	0.90	0.90
		B	1.09	1.10	1.09	1.10	1.09
2.0	TIN_based	*N*	0.77	0.77	0.77	0.77	0.77
		R	0.91	0.91	0.91	0.91	0.91
		B	1.31	1.32	1.31	1.32	1.31
	Improved algorithm	*N*	0.81	0.80	0.81	0.81	0.80
		R	0.90	0.90	0.90	0.90	0.90
		B	1.08	1.06	1.10	1.09	1.07
2.5	TIN_based	*N*	0.77	0.77	0.77	0.77	0.77
		R	0.91	0.91	0.91	0.91	0.91
		B	1.31	1.31	1.32	1.32	1.32
	Improved algorithm	N	0.81	0.81	0.81	0.81	0.80
		R	0.90	0.90	0.90	0.90	0.90
		B	1.08	1.09	1.09	1.10	1.08

https://doi.org/10.5194/gmd-2022-92
Preprint. Discussion started: 24 May 2022

Geoscientific Model Development Discussions

Table 5: Three statistical indicators from the SWAT model and improved algorithm under a flow source point scale of 30 m at the outlet of the BBW.

Algorithm	Statistical indicators		
	N	*R*	*B*
SWAT	0.41	0.87	0.96

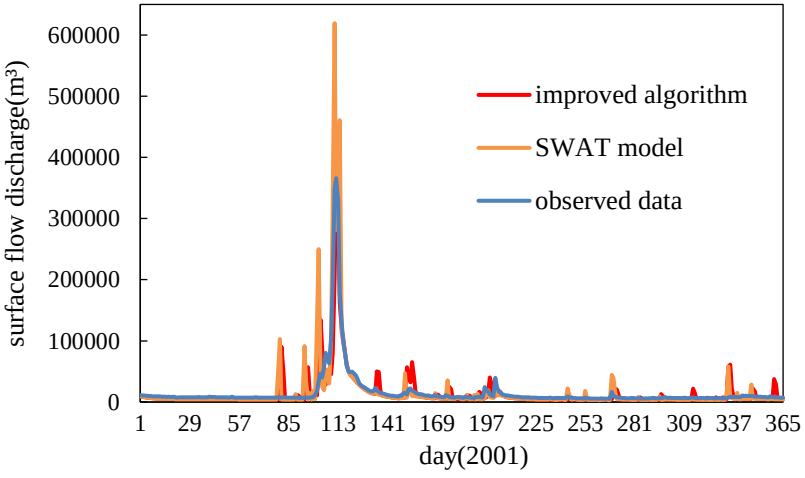

Figure 8: The surface flow discharge simulated from the SWAT model and improved algorithm at the outlet of BBW (threshold of retrieving the critical points was 0.5 m, and scale of the flow source points was 30 m).

The experiments to evaluate the computational efficiency of the improved method were performed on a desktop computer with an i7-6800 CPU, 64 GB RAM, 500 GB SSD, 1080 NVIDIA GeForce GTX (computational ability of 2.1 and number of SMs of 20) and Microsoft Windows 10 using the 64-bit option. Table 6 summarizes the computing times by changing the threshold value of retrieving the critical points and the scale of flow source points for the TIN_based and improved algorithms.

https://doi.org/10.5194/gmd-2022-92
Preprint. Discussion started: 24 May 2022

Geoscientific Model Development Discussions

Table 6: The calculation times obtained by varying the threshold value of retrieving the critical points and the scale of flow source points for the TIN_based and improved algorithms (Unit: second).

Threshold/m	Algorithm	Scale of flow source points/m				
		10	15	20	25	30
0.5	TIN_based	953.82	425.37	278.18	213.77	169.77
	Improved algorithm	60.93	30.47	22.26	17.36	16.29
1.0	TIN_based	912.16	407.40	278.21	203.25	159.87
	Improved algorithm	60.00	31.48	20.45	17.04	16.04
1.5	TIN_based	899.07	395.99	267.96	196.33	159.60
	Improved algorithm	57.91	30.57	20.02	17.50	16.12
2.0	TIN_based	893.92	396.22	270.80	198.07	159.21
	Improved algorithm	58.92	29.36	21.48	18.01	16.33
2.5	TIN_based	892.59	400.38	260.40	199.60	164.56
	Improved algorithm	56.86	29.52	19.64	16.80	15.50

In addition, to verify the multiscale expression effect of this method, the improved method was utilized to simulate the surface flow discharges at different temporal and spatial scales. In terms of time scale, the proposed method estimates the flow velocity along the flow line through the improved Manning formula and combines it with the predetermined travel time to predict the surface flow movement distance and surface flow discharge at this time. Therefore, the improved algorithm is used to simulate the surface flow discharge under different times of 1, 2, 3..., 2250 s. Figure 9 shows the real-time changes of surface flow discharge simulated by the proposed algorithm (threshold of retrieving the critical points was 0.5 m and scale of flow source points was 30 m) at the three locations (upstream point, middle point and downstream point) represented by the blue, green and red points in Fig. 3.

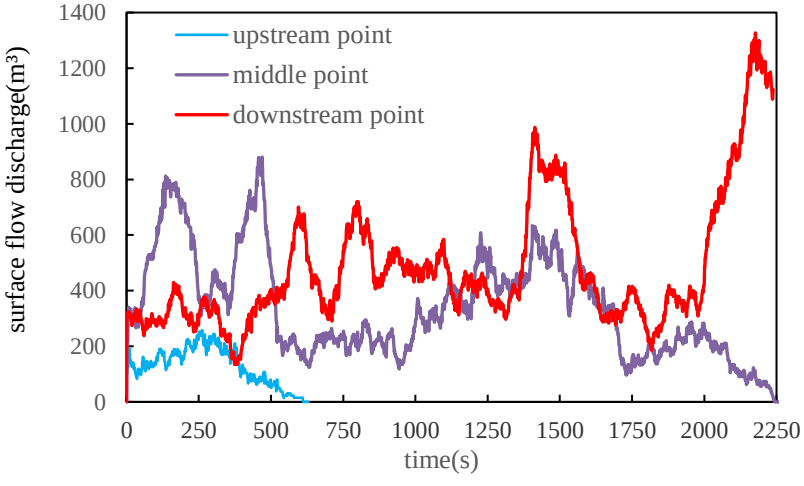

Figure 9: Real-time changes in surface flow discharge simulated by the proposed algorithm (threshold of retrieving the critical points was 0.5 m and scale of flow source points was 30 m) at three locations (upstream point, middle point and downstream point).

In terms of spatial scale, the scale attributes of critical points under different threshold values were assigned according

https://doi.org/10.5194/gmd-2022-92
Preprint. Discussion started: 24 May 2022

Geoscientific Model Development Discussions

to the correspondence between the maximum elevation error (Emax), RMSE and scale. Table 7 describes the national standard between scale, spatial resolution, Emax and RMSE. Emax is equal to the threshold of retrieving the critical points by the parallel-multipoint algorithm. Therefore, Emax can be used to obtain the critical points at a given scale (or resolution). For example, when Emax is 0.4 m, if RMSE is less than 0.2 m, then the scale of the retrieved critical points is 0.5 m (or 1:1,000); when Emax is 6.0 m, if RMSE is less than 3.0 m, then the scale of the retrieved critical points is 7.5 m (or 1:15,000).

Table 7: The national standard between scale, spatial resolution, Emax and RMSE.

Scale	1:1000	1:5000	1:10,000	1:15,000	1:20,000	1:25,000	1:50,000
Resolution/m	0.5	2.5	5.0	7.5	10.0	12.5	25.0
RMSE/m	0.2	1.0	2.0	3.0	4.0	5.0	10.0
Emax/m	0.4	2.0	4.0	6.0	8.0	10.0	20.0

Data source: State Bureau of Quality and Technical Supervision of China (2000, 2001).

The drainage-constrained TINs constructed under the different threshold values (Emax values) of retrieving the critical points from the no-depression DEM were compared with the original DEM to obtain the RMSE of different TINs, as shown in Table 8. The optimal fitting formula was obtained by correlating Emax with RMSE. According to the fitting formula, the thresholds of retrieving the critical points corresponding to different RMSEs (0.2, 1.0 and 2.0 m) are shown in Table 9. From Table 9, we can see that when the threshold of retrieving the critical points is 0.59, 3.27 and 4.99 m, the RMSE of drainage-constrained TINs is 0.2, 1.0 and 1.3 m, respectively. Combined with Table 8, the corresponding scale of the critical points was 1:1,000 (0.5 m), 1:5,000 (2.5 m) and 1:10,000 (5.0 m). Figure 10 shows the retrieved critical points and the drainage-constrained TINs with different scales.

Table 8: The number of critical points, the number of triangular facets over TIN and the corresponding RMSE.

Emax/m	0.5	1.0	1.5	2.0	2.5
points [a]	10,859	4,295	2,149	1,268	822
triangulars [b]	23,348	11,079	6,854	5,139	4,285
RMSE/m	0.17	0.31	0.45	0.58	0.73

[a] Number of retrieved critical points; [b] Number of triangular facets over TIN.

Table 9: The number of critical points, the number of triangular facets over TIN and the corresponding RMSE.

fitting formula	R^2	RMSE/m		
		0.2	1.0	2.0
$r = 0.014t^3 - 0.0601t^2 + 0.3491t + 0.0127$	0.9999	0.59	3.27	4.99

https://doi.org/10.5194/gmd-2022-92
Preprint. Discussion started: 24 May 2022

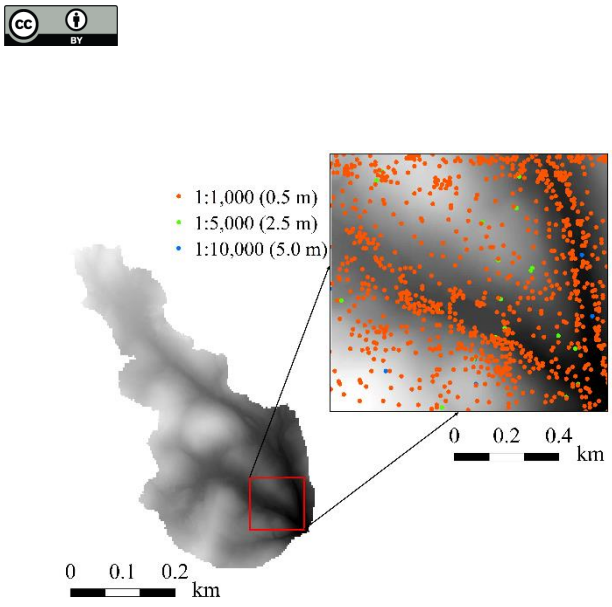

(a) the critical points with different scales

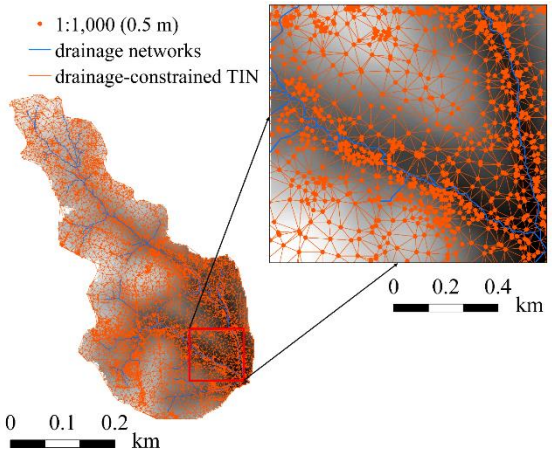

(b) the drainage-constrained TIN of 1:1,000

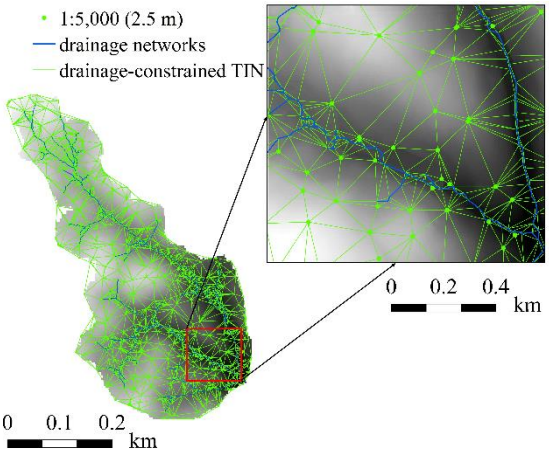

(c) the drainage-constrained TIN of 1:5,000

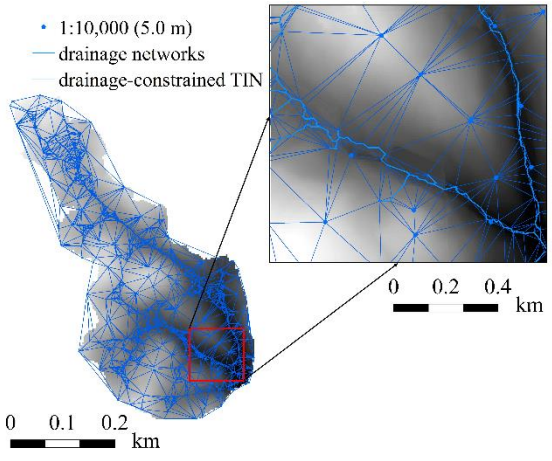

(d) the drainage-constrained TIN of 1:10,000

Figure 10: The retrieved critical points and the drainage-constrained TINs with different scales.

Combined with the flow source points at scales of 10, 15, 20, 25 and 30 m, the improved method was utilized to simulate the daily surface flow discharge at the outlet of the BBW under different scales of TIN and flow source points. The accuracy of the simulation results was evaluated as shown in Table 10. In addition, the simulation results from the improved method at different scales of TIN and a flow source point scale of 30 m were compared with those of the simulation results from the SWAT model, as shown in Fig. 11.

https://doi.org/10.5194/gmd-2022-92
Preprint. Discussion started: 24 May 2022

Geoscientific Model Development Discussions

Table 10: The accuracy of the improved method under different scales of TIN and flow source points.

Scale of TIN/m	Statistical indicators	Scale of the flow source points/m				
		10	15	20	25	30
0.5	*N*	0.808	0.806	0.800	0.800	0.809
	R	0.899	0.899	0.896	0.896	0.900
	B	1.079	1.078	1.063	1.063	1.085
2.5	*N*	0.804	0.809	0.807	0.810	0.805
	R	0.898	0.900	0.899	0.901	0.898
	B	1.075	1.088	1.082	1.091	1.077
5.0	*N*	0.809	0.805	0.811	0.805	0.811
	R	0.900	0.898	0.901	0.898	0.902
	B	1.087	1.078	1.094	1.078	1.095

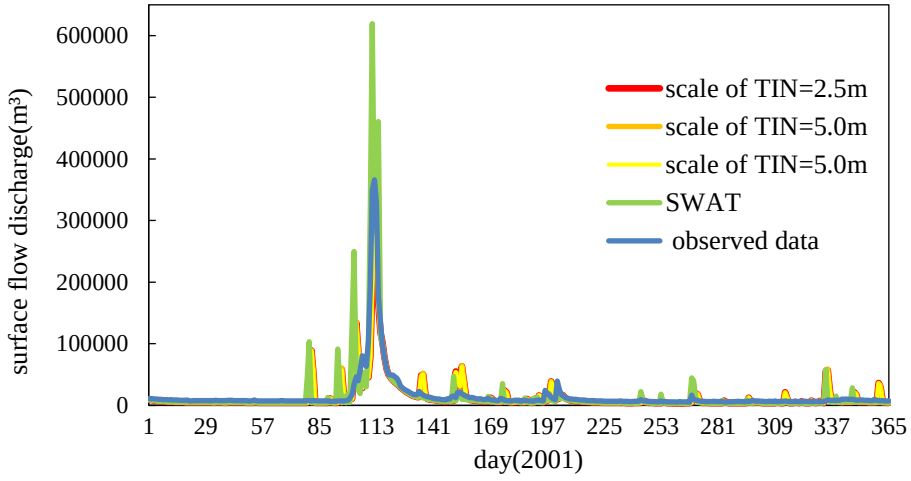

375 **Figure 11: The surface flow discharge from the SWAT model and the improved method at the outlet of BBW (scale of the flow source points was 30 m).**

4. Discussion

The improved algorithm aimed to efficiently use the flow path network to simulate the surface flow discharge with high accuracy at any temporal and spatial scale. Therefore, we not only use the Nash efficiency (*N*), correlation coefficient (*R*) 380 and balance coefficient (*B*) to evaluate the accuracy between the improved algorithm and two existing methods and the multiscale expression effect of the improved method but also employ time statistics to assess the computational efficiency of the improved method.

https://doi.org/10.5194/gmd-2022-92
Preprint. Discussion started: 24 May 2022

Geoscientific Model Development Discussions

4.1 Accuracy and computing performance enhancement measures

As seen from Table 4, with the increase of scale of the flow source points, when the thresholds of retrieving the critical points are 0.5, 1.0, 1.5, 2.0 and 2.5 m, the *N*, *R* and *B* value of the TIN_based method is 0.77, 0.91 and 1.30 to 1.32, respectively. The *N*, *R* and *B* values of the improved method are between 0.80 and 0.82, between 0.90 and 0.91 and between 1.06 and 1.11, respectively. With the change of threshold of retrieving the critical points and scale of flow source points, the *N* value increases by 6.49%, the *R* value decreases by 1.10% and the *B* value increases by 19.08%. Therefore, the improved method has a higher simulation accuracy.

Combining Fig. 8 and Table 5, the simulation results of the improved method are closer to the measured data from the observation station and better than the simulation results of the SWAT model. The Nash coefficient increases by 97.56%. The correlation coefficient increases by 4.60%. The balance coefficient is very close to 1. The SWAT model divides the watershed into hydrological response units (HRUs) and uses its unique combination of land cover, slope and soil type for the surface flow dynamics simulation. The model has many input parameters to an uncertain simulation result, and its accuracy depends on the DEM resolution. Therefore, the accuracy of the improved method is significantly enhanced and can avoid the influence of parameters and DEM resolution on the accuracy.

Figure 12 shows the speedup ratio of the improved method at different thresholds of retrieving the critical points and different scales of flow source points. With the decrease in the scale of the flow source points, the speedup ratio under the thresholds of 0.5 m reaches 15.7. When the threshold of retrieving the critical points is 1.0 m, the speedup ratio reaches 15.2. When the threshold of retrieving the critical points is 1.5 m, the speedup ratio reaches 15.5. When the threshold of retrieving the critical points is 2.0 m, the speedup ratio reaches 15.2. When the threshold of retrieving the critical points is 2.5 m, the speedup ratio reaches 15.7. This demonstrates that the computing efficiency of the improved method is greatly enhanced, and the speedup ratio reaches 15.7.

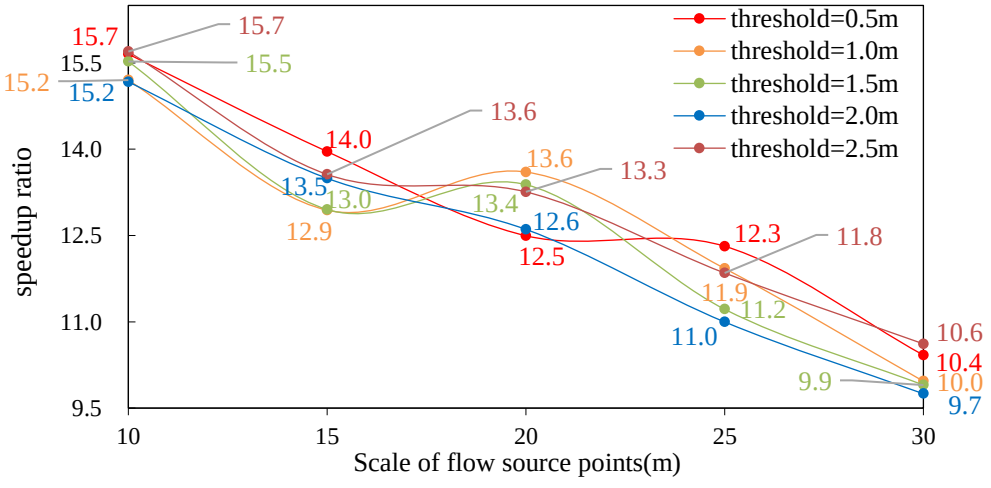

Figure 12: The speedup ratio of the improved method at different thresholds of retrieving the critical points and different scales of flow source points.

https://doi.org/10.5194/gmd-2022-92
Preprint. Discussion started: 24 May 2022


Geoscientific Model Development Discussions

4.2 Multiscale expression effect

As shown in Fig. 7, the flow discharges of the three locations are low because the flow has not begun at 0 seconds. Then, the flow discharge accumulated with the change in time. The flow at the upstream points shows a gentle-low curve and stops at 600 seconds for the small catchment area and short flow line. At the middle point, the flow curve fluctuates from approximately 100 seconds to approximately 2000 seconds because the different travel times result in the upstream flow to different places. After approximately 250 seconds, all the flow discharge subsides and goes out to zero. In addition, the flow discharge at the middle point is generally higher than that at the upstream point because of its larger catchment area and longer flow line.

At the downstream point, the flow curve is similar to that of the middle point, but the sections of low flow discharge and high flow discharge are opposite to that of the middle point. Because the time is small, more upstream discharge cannot flow into this position, while when the time is large, more upstream discharge can flow into this position. The curve of the downstream point reached the maximum value at approximately 2100 seconds for a large catchment area and long flow accumulation time. Based on the analysis of the mechanism of surface flow dynamic simulation, these results are consistent with the actual expected results. Thus, the improved method can simulate the surface flow dynamics in real time.

As seen from Table 5 and Table 10, compared with the SWAT model, the *N* value of the improved method increases by 95%, and the *R* value increases slightly by approximately 3%. In addition, the *B* value is very close to 1. Combined with Fig. 11, both the improved method and SWAT model can simulate the surface flow discharge at the outlet of the BBW, but the simulation curve of the improved model is closer to the measured data than that of the SWAT model. Therefore, the multiscale simulation accuracy of the improved method is significantly enhanced.

Drainage-constrained TINs with different scales can be conveniently constructed based on different scales of critical points. The flow source points, a collection of arbitrary surface points, are not related to the scale of the TIN, so the scale of the flow source points is separated from that of the TIN. This solves the problem that the simulation cell of the traditional surface flow discharge method is consistent with the grid cell of the DEM and the computing amount is large and complex. The traditional hydrological methods almost regard the DEM grid cells or HRUs in the SWAT model as the simulation cells.

These simulation cells have a planar geometry, and it is difficult to express the simulation of any point on the surface. However, multiscale surface flow dynamics simulation by the improved method can express the simulation result of any point on the surface to improve the simulation accuracy from the planar level to the point level. Therefore, the simulation accuracy is better improved, and the surface flow dynamic simulation under different temporal and spatial scales can be realized. In addition, according to Table 4 and Table 10, while improving the simulation accuracy of the improved method, the *N* values fluctuate in a small range of approximately 0.80, the *R* values fluctuate in a small range of approximately 0.90 and the *B* values fluctuate in a small range of approximately 1.08. Therefore, the multiscale simulation results of the improved algorithm do not vary greatly because the scale of the TIN and flow source points remain consistent.

https://doi.org/10.5194/gmd-2022-92
Preprint. Discussion started: 24 May 2022

4.3 Limitations and future enhancements

As described in this paper, we only consider the influence of three terrain parameters on the surface flow velocity to improve Manning's equation. Other terrain parameters (such as upslope area and upslope slope) also have an impact on the flow velocity, and we will further discuss the influence of other terrain parameters on the accuracy of simulating the surface flow dynamics. In addition, the improved method only implemented the parallelization of retrieving the critical points algorithm during the construction of drainage-constrained TINs. The parallelization of the TIN construction algorithm and D8 algorithm are not considered in current research. We also hope to parallelize the two algorithms and form a complete set of parallel algorithms for constructing the drainage-constrained TIN based on CUDA. Research will also focus on the derivation of different terrain parameters and the surface flow dynamic simulation method with higher accuracy and computational efficiency to satisfy the needs of more users.

5. Conclusions

To solve the problems of the accuracy and real-time response efficiency of the existing surface flow dynamic simulation algorithms, an improved algorithm was proposed to simulate the surface flow dynamics quickly and accurately to meet the requirements of accurate and immediate response in practical applications. In the improved algorithm, the critical points retrieved from the high-resolution grid DEM by the parallel-multi-point algorithm and the drainage networks extracted by the D8 algorithm were combined to construct the drainage-constrained TIN first. Then, the flow direction of each triangular facet on the TIN was calculated by the aspect and slope of the triangular facet. The flow lines from the flow source points to the outlet were tracked by combining the randomly sampled flow source points with the flow direction to simplify the three-dimensional surface into a one-dimensional flow path network (FPN).

On this basis, the slope length factor and flow path curvature were obtained from the DEM by using the FPN_L and FPN_FPC methods. The topographic wetness index was acquired from the DEM by a new algorithm. Then, based on the analytic hierarchy process (AHP), the classical Manning formula was improved by using the slope length factor, topographic wetness index and flow path curvature to accurately estimate the velocity of each flow line over the FPN. Finally, CUDA was utilized to parallelize the flow velocity estimation function and surface flow discharge count function on the flow lines over the FPN. Combined with the preset travel time, the movement distance was predicted, and the surface flow discharge was simulated at any location to complete the dynamic simulation of surface water at any time. The proposed algorithm improved the Manning formula to enhance the accuracy and used CUDA to advance the real-time response efficiency.

To verify the accuracy and computing efficiency of the improved algorithm, the simulation results and calculation time were compared with the TIN_based algorithm under different thresholds of retrieving the critical points and different scales of flow source points. In addition, the simulation results of the proposed algorithm were compared with those of the SWAT model at a flow source point scale of 30 m to further verify its accuracy. The experimental results show that, compared with the TIN_based algorithm, the Nash coefficient increases by 6.49%, the correlation coefficient decreases slightly and the

https://doi.org/10.5194/gmd-2022-92
Preprint. Discussion started: 24 May 2022

balance coefficient increases by 19.08%. Compared with the SWAT model, the Nash coefficient increased by 97.56% and the correlation coefficient increased by 4.60%. The balance coefficient of the proposed algorithm is close to 1 and outperforms other existing algorithms.

Compared with the TIN_based method, the computing efficiency is greatly improved, and the speedup ratio reaches 15.7. The Nash coefficient, correlation coefficient and balance coefficient of the improved algorithm fluctuate within a small range of 0.81, 0.90 and 1.09. Moreover, the improved algorithm can simulate surface flow dynamics in real time, and the multiscale simulation results do not vary greatly with the scale of the TIN and flow source points. Therefore, the improved algorithm can quickly and accurately complete the multiscale surface flow dynamic simulation and ensure the consistency of simulation results.

Code Availability

The code had been archived in the Zenodo and its URL is https://doi.org/10.5281/zenodo.6543680. The code still needs to be improved and will be updates when it's perfect.

Data Availability

The image data and the daily rainfall data are confidential data which were derived from the cooperation project and not publicly available for the time being.

Author contribution

Qianjiao Wu and Yumin Chen design the experiments and carried them out. Qianjiao Wu, Huaming Xie and Tong Xu developed the model code. Qianjiao Wu, Ting Zhang and Jiayong Yu prepared the manuscript with contributions from all co-authors. Yumin Chen and Huaming Xie revised the manuscript and given final approval of the version to be published.

Competing interests

The authors declare that they have no conflict of interest.

Acknowledgements

This work was supported by the Research Fund of Anhui Jianzhu University [grant number 2021QDZ01, 2020QDZ35], the National Natural Science Foundation of China [grant number 42106180], Natural Science Research Project of University in Anhui Province [grant number KJ2019A0763] and the Natural Science Foundation of Anhui Province [grant number

https://doi.org/10.5194/gmd-2022-92
Preprint. Discussion started: 24 May 2022


Geoscientific Model Development Discussions

2108085QD151].

References

Arnold, J. G., Srinicasan, R., Muttiah, R. S. and Williams, J. R.: Large area hydrologic modeling and assessment part I: model development, J. Am. Water Resour. Assoc., 34(1), 73–89, https://doi.org/10.1111/j.1752-1688.1998.tb05961.x, 1998.

Beven, K., Warren, R. and Zaoui, J.: SHE: towards a methodology for physically-based distributed forecasting in hydrology, Hydrol. Forecast. (IAHS Publ., 129, 133–137, 1980.

Beven, K. J. and Kirkby, M. J.: A physically based, variable contributing area model of basin hydrology, Hydrol. Sci. Bull., 24, 43–69, 1979.

Blaszczak-Bak, W., Artur Janowski and Piotr Srokosz: High performance filtering for big datasets from Airborne Laser Scanning with CUDA technology, Surv. Rev., 50(360), 262–269, https://doi.org/10.1117/12.833740, 2018.

Bourdin, D. R., Fleming, S. W. and Stull, R. B.: Streamflow Modelling: A Primer on Applications, Approaches and Challenges, Atmosphere-Ocean, 50(4), 507–536, https://doi.org/10.1080/07055900.2012.734276, 2012.

Chaney, N. W., Herman, J. D., Reed, P. M. and Wood, E. F.: Flood and drought hydrologic monitoring: The role of model parameter uncertainty, Hydrol. Earth Syst. Sci., 19(7), 3239–3251, https://doi.org/10.5194/hess-19-3239-2015, 2015.

Chen, Y., Zhou, Q., Li, S., Meng, F., Bi, X., Wilson, J. P., Xing, Z., Qi, J., Li, Q. and Zhang, C.: The simulation of surface flow dynamics using a flow-path network model, Int. J. Geogr. Inf. Sci., 28(11), 2242–2260, https://doi.org/10.1080/13658816.2014.917312, 2014.

Costa-Cabral, M. C. and Burges, S. J.: Digital Elevation Model Networks (DEMON): A model of flow over hillslopes for computation of contributing and dispersal areas, Water Resour. Res., 30(6), 1681–1692, https://doi.org/10.1029/93wr03512, 1994.

David, L. and Frank, L.: High-resolution geomorphological map of a low mountain range near Aachen, Germany, J. Maps, 9, 245–253, https://doi.org/10.1080/17445647.2013.771291, 2013.

Djokic, D. and Maidment, D. R.: Application of GIS network routines for water flow and transport, J. Water Resour. Plan. Manag., 119(2), 3456, https://doi.org/10.1061/(ASCE)0733-9496(1993)119:2(229), 1993.

Easterling, D. R., Evans, J. L., Groisman, P. Y., Karl, T. R., Kunkel, K. E. and Ambenje, P.: Observed variability and trends in extreme climate events: A brief review, Bull. Am. Meteorol. Soc., 81(3), 417–426, https://doi.org/10.1175/1520-0477(2000)081<0417:OVATIE>2.3.CO;2, 2000.

Glenn, O. and Ashton, S.: Quantifying local flow direction uncertainty, Int. J. Geogr. Inf. Sci., 27(7), 1292–1311, https://doi.org/10.1080/13658816.2012.719627, 2012.

Guide, N. C.: CUDA C Programming Guide, edited by Santa Clara, Taylor & Francis, CA,USA., 2015.

Ivanov, V. Y., Vivoni, E. R., Bras, R. L. and Entekhabi, D.: Preserving high-resolution surface and rainfall data in operational-scale basin hydrology: a fully-distributed physically-based approach, J. Hydrol., 298(1–4), 80–111, https://doi.org/10.1016/j.jhydrol.2004.03.041, 2004.

Hellmers S. and Fröhle P.: Computation of backwater effects in surface waters of lowland catchments including control structures–an efficient and re-usable method implemented in the hydrological open-source, Geosci. Model Dev., 15, 1061–1077, https://doi.org/10.5194/gmd-15-1061-2022, 2022.

Jia, Y., Wang, H., Ni, G., Yang, D., Wang, J. and Qin, D.: Principles and practice of distributed watershed hydrological modeling, China WaterPower Press, Beijing., 2005.

Kuffour, B. N. O, Engdahl N. B., Woodward, C. S., Condon, L. E., Kollet S., and Maxwell R. M.: Simulating coupled surface–subsurface flows with ParFlow v3.5.0: capabilities, applications, and ongoing development of an open-source, massively parallel, integrated hydrologic model, Geosci. Model Dev., 13, 1373–1397, https://doi.org/10.5194/gmd-13-1373-2020, 2020.

López-Vicente, M., Navas, A., Gaspar, L. and Machín, J.: Impact of the new common agricultural policy of the EU on the runoff production and soil moisture content in a Mediterranean agricultural system, Environ. Earth Sci., 71(10), 4281–4296, https://doi.org/10.1007/s12665-013-2790-4, 2013.

Maneta, M. P. and Wallender, W. W.: Pilot-point based multi-objective calibration in a surface-subsurface distributed hydrological model, Hydrol. Sci. J., 58(2), 390–407, https://doi.org/10.1080/02626667.2012.754987, 2013.

Manning, R.: On the Flow of Water in Open Channels and Pipes, Trans. Inst. Civ. Eng. Irel., 20, 161–209, 1891.

O'Callaghan, J. F. and Mark, D. M.: The extraction of drainage networks from digital elevation data, Comput. Vision, Graph. Image Process., 28, 328–344, https://doi.org/10.1016/S0734-189X(84)80011-0, 1984.

Olivera, F. and Maidment, D. R.: "Chapter 5: GIS tools for HMS modeling support. "Hydrologic and hydraulic modeling support with geographic information systems, Maidment D. R. and Djokic D., eds., ESRI Press, Redlands, Calif, 85-112, 2000.

Puppo, D., Davis, L., De Menthon, D. and A. Teng, Y.: Parallel terrain triangulation, Int. J. Geogr. Inf. Syst., 8(2), 105–128, https://doi.org/10.1080/02693799408901989, 1994.

Qu, Y. and Duffy, C. J.: A semidiscrete finite volume formulation for multiprocess watershed simulation, Water Resour. Res., 43(8), W08419, https://doi.org/10.1029/2006wr005752, 2007.

Shen, X., Wang, L. and Xie, S.: A dynamic precipitation-runoff model for a watershed based on grid data, Acta Geographica Sinica, 50(3), 264–271, https://doi.org/10.11821/xb199503009, 1995.

Staškovanová, V. and Minár, J.: Modelling the geomorphic history of the Tribeč Mts. and the Pohronský Inovec Mts. (Western Carpathians) with the CHILD model, Open Geosci., 8(1), 371–389, https://doi.org/10.1515/geo-2016-0038, 2016.

Swarnkar, S., Malini, A., Tripathi, S. and Sinha, R.: Assessment of uncertainties in soil erosion and sediment yield estimates at ungauged basins: an application to the Garra River basin, India, Hydrol. Earth Syst. Sci., 22(4), 2471–2485, https://doi.org/10.5194/hess-22-2471-2018, 2018.

560 Tachikawa, Y. and Takasao, T.: TIN-based topographic modelling and runoff prediction using a basin geomorphic information system, HydroGIS 96 Appl. Geogr. Inf. Syst. Hydrol. Water Resour. Manag. (Proceedings Vienna Conf. April 1996). IAHS Publ. 235, 1996.

Tachikawa, Y., Shiiba, M. and Takasao, T.: Development of a basin geomorphic information system using a TIN-DEM data structure, Water Resour. Bull. Am. Water Resour. Assoc., 30(1), 9–17, https://doi.org/10.2208/prohe.36.677, 1994.

565 Thavhana, M. P., Savage, M. J. and Moeletsi, M. E.: SWAT model uncertainty analysis, calibration and validation for runoff simulation in the Luvuvhu River catchment, South Africa, Phys. Chem. Earth, Parts A/B/C, 105, 115–124, https://doi.org/10.1016/j.pce.2018.03.012, 2018.

Thompson, S. A.: Hydrology for Water Management, Rotterdam: A Balkema., 1999.

Tucker, G. E., Lancaster, S. T., Gasparini, N. M. and Bras, R. L.: The Channel-Hillslope Integrated Landscape Development
570 Model (CHILD) model, in Harmon, R.S., Doe, W. (eds.), Landscape Erosion and Evolution Modelling, pp. 349–388, Kluwer Academic/Plenum Publishers, Dordrecht., 2001.

Wilson, J. P. and Gallant, J. C.: Terrain Analysis: Principles and Applications, John Wiley & Sons, Inc, New York, USA., 2000.

Wu, Q. and Chen, Y.: A Parallel Method of Surface Flow Dynamics Simulation based on CUDA, J. Geo-information Sci.,
575 22(3), 505–515, https://doi.org/10.12082/dqxxkx.2020.190500, 2020.

Wu, Q., Chen, Y., Wilson, J. P., Liu, X. and Li, H.: An effective parallelization algorithm for DEM generalization based on CUDA, Environ. Model. Softw., 114, 64–74, https://doi.org/10.1016/j.envsoft.2019.01.002, 2019.

Wu, Q., Chen, Y., Zhou, H., Chen, S. and Wang, H.: A new algorithm for calculating the flow path curvature (C) from the square-grid digital elevation model (DEM), ISPRS Int. J. Geo-Inf., 9(9), 32–34, https://doi.org/10.3390/ijgi9090510, 2020.

580 Wu, Q., Chen, Y., Wilson, J. P., Tan, H. and Chu, T.: A new approach for calculating the slope length factor in the Revised Universal Soil Loss Equation, J. Soil Water Conserv., 76(2), 153–165, https://doi.org/10.2489/jswc.2021.00085, 2021.

Zhang, F., Zhou, Q., Li, Q., Wu, G. and Liu, J.: a High-Performance Method for Simulating Surface Rainfall-Runoff Dynamics Using Particle System, ISPRS Ann. Photogramm. Remote Sens. Spat. Inf. Sci., III–2(July), 109–112, https://doi.org/10.5194/isprsannals-iii-2-109-2016, 2016.

585 Zhang, F., Zhou, Q., Li, Q., Wu, G. and Liu, J.: An enhanced approach for surface flow routing over drainage-constrained triangulated irregular networks, Trans. GIS, 22(1), 43–57, https://doi.org/10.1111/tgis.12294, 2018.

Zhou, G., Liu, X., Fu, S. and Sun, Z.: Parallel identification and filling of depressions in raster digital elevation models, Int. J. Geogr. Inf. Sci., 31(6), 1061–1078, https://doi.org/10.1080/13658816.2016.1262954, 2017.

Zhou, Q. and Chen, Y.: Generalization of DEM for terrain analysis using a compound method, ISPRS J. Photogramm.
590 Remote Sens., 66(1), 38–45, https://doi.org/10.1016/j.isprsjprs.2010.08.005, 2011.

Zhou, Q. and Liu, X.: Error analysis on grid-based slope and aspect algorithms, Photogramm. Eng. Remote Sens., 70(8), 957–962, https://doi.org/10.14358/PERS.70.8.957, 2004.

Zhou, Q. and Liu, X.: Digital Terrain Analysis, Science Press, Beijing, 2006.

https://doi.org/10.5194/gmd-2022-92
Preprint. Discussion started: 24 May 2022

Zhou, Q., Pilesjö, P. and Chen, Y.: Estimating surface flow paths on a digital elevation model using a triangular facet network, Water Resour. Res., 47(7), https://doi.org/10.1029/2010WR009961, 2011.